**Supplementary Information**

# A gas-phase amplified quartz crystal microbalance immunosensor based on catalase modified immunoparticles

Wei Liu [a], Renliang Huang [b], Wei Qi [a, c, d,]*, Mengfan Wang [a, d], Rongxin Su [a, c, d] and Zhimin He [a]

[a] State Key Laboratory of Chemical Engineering, School of Chemical Engineering and Technology, Tianjin University, Tianjin, 300072, China

[b] School of Environmental Science and Engineering, Tianjin University, Tianjin, 300072, China

[c] The Co-Innovation Center of Chemistry and Chemical Engineering of Tianjin, 300072, China

[d] Tianjin Key Laboratory of Membrane Science and Desalination Technology, Tianjin, 300072, China

* Corresponding author. Phone: +86 22 27407799. E-mail address: qiwei@tju.edu.cn

## 1. Photograph of the QCM analysis system

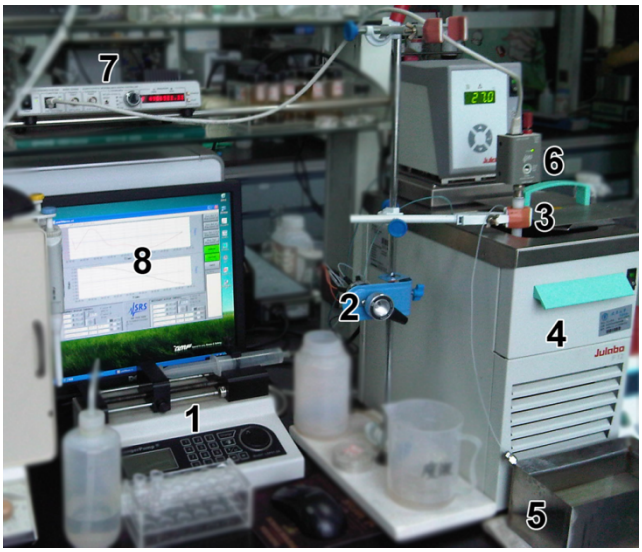


**Fig. S1** Photograph of the QCM analysis system. Carrier solution was pumped by 1) a syringe pump and traveled through the flow channel which consists of 2) a 6-port sample injector, 3) a flow cell immersed in 4) a temperature controller, and 5) a waste container. QCM sensor was placed in the flow cell and driven by 6) a QCM25 Crystal Oscillator. Sensor signal was collected by 7) a QCM200 Digital Controller and displayed, analyzed and stored by 8) a SrsQcm200 software.

## 2. SEM and TEM characterizations of the MSCA

For scanning electron microscope (SEM), the 150 nm magnetic nanoparticle and synthesized MSCA were sputter-coated with platinum using an E1045 Pt-coater (Hitachi High-technologies CO., Japan) and then imaged by an S-4800 field emission scanning electron microscope (SEM, Hitachi High-technologies CO., Japan) at an acceleration voltage of 3.0 kV. Increase of the surface roughness as shown in **Fig. S-2** was induced by protein modification.

Transmission electron microscopy (TEM) images were obtained on a JEM100CXII (JEOL, Japan) transmission electron microscope, using an accelerating voltage of 100 kV. Negative staining by 1.0% phosphotungstic acid for 2 min was applied to enhancing the contrast of particle edges which were covered by proteins.

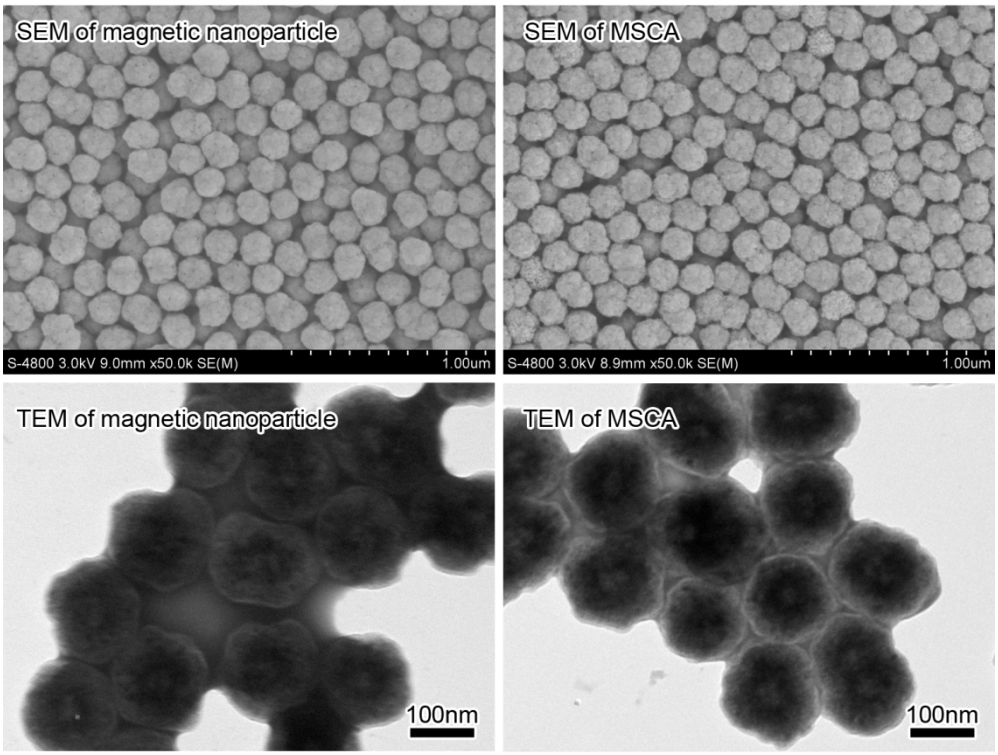


**Fig. S2** SEM and TEM images of the 150 nm magnetic nanoparticle and MSCA.

## 3. The small frequency shift caused by MSCA binding

Viscous (nonrigid) coupling of liquid medium to the QCM sensor surface results not only in a decrease in the frequency ($\Delta f$) but also in damping of resonant oscillation, which is manifested as an increase in resistance ($\Delta R$). Thus, the resistance shift can be served as an independent indicator of the rigidity of the layer formed on the QCM sensor surface.[1]

In **Fig. S3a**, the frequency shifts were obtained from the typical sensorgram (**Fig. 3**); the corresponding resistance shifts were recorded by the QCM200 along with the frequency recording. As can be seen from the

data, the progress could be divided into four steps including: 1) IgG capture by the anti-IgG antibody immobilized on the QCM sensor surface; 2) association/dissociation equilibration of the interaction between IgG and anti-IgG antibody; 3) dissociation of the interaction; and 4) MSCA capture by the already captured IgG.

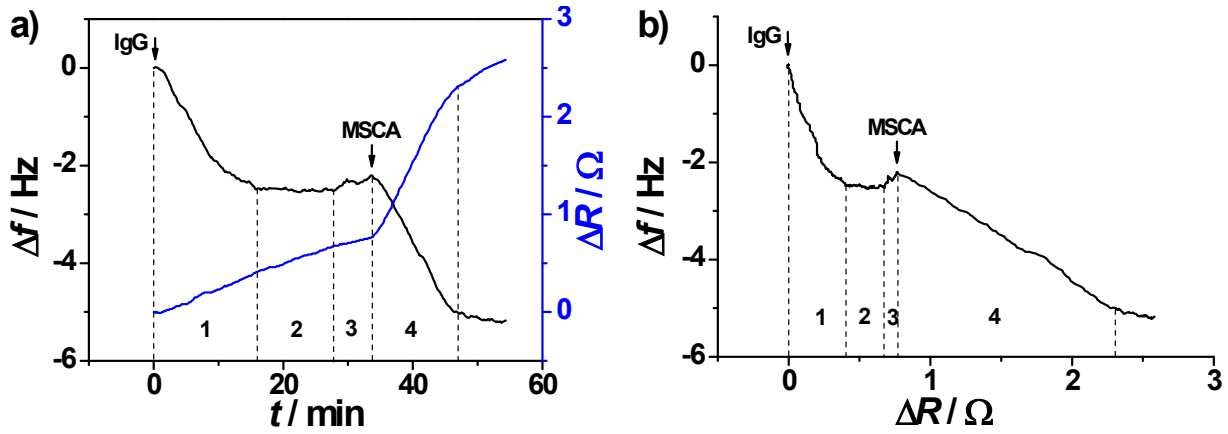


**Fig. S3** a) Frequency and resistance responses caused by QCM detection of 0.3 μg $ml^{-1}$ IgG and MSCA amplification. b) Frequency shift *vs.* resistance shift curve reproduced from a).

In the step 1 of **Fig. S3a**, a fast frequency drop and a slow resistance increase were observed. While in the step 4, both the frequency and the resistance were changed fast. These differences could be further verified in **Fig. S3b**, in which the curve slopes of steps 1 and 4 were -5.89 Hz/Ω and -1.83 Hz/Ω, respectively. These results have indicated that the layer formed by the MSCA capture was less rigid than that formed by the IgG capture.[2-4] Therefore, it is reasonable to assume that the small frequency shift caused by MSCA binding is, to some extent, due to small rigidity of the sandwich-type complex.

## 4. Structure analysis and optimization of the flow cells

To understand the sudden signal shift in **Fig. 4c**, the structure of the axial flow chamber was reproduced by SolidWorks software (**Fig. S4 A1**), and then its flow pattern was analysed by computational fluid dynamics simulation (with flow simulation plug-in of SolidWorks software). Boundary conditions of the simulation were as follows: inlet volume flow velocity was 30 μL $min^{-1}$; outlet condition was atmosphere pressure; temperature of the fluid (water) was 37 °C.

As can be seen from the simulation results (**Fig. S4 A3 and A4**), the flow velocity in the chamber was extremely nonuniform. Because the edge region of the flow chamber was much larger than the center region, the flow velocity in the edge region was so small that a fluid dead zone was likely formed. In this study, we believe that the formation of a fluid dead zone is one of the reasons which caused the sudden signal of **Fig. 4c**, and as a result should be eliminated.

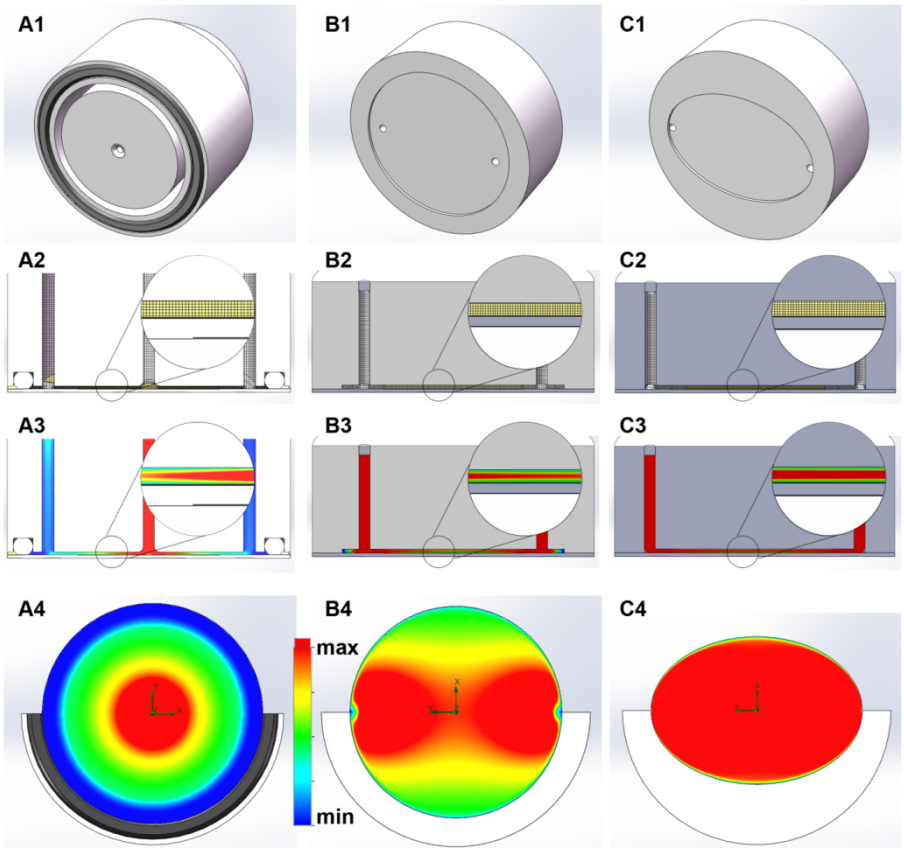


**Fig. S4** A1, B1, and C1 were structures of the axial flow chamber, the most commonly used lateral flow chamber, and the homemade lateral flow chamber, respectively. A2, B2, and C2 represented meshes generated in the simulations. A3, B3, C3, A4, B4, and C4 showed flow velocity distributions on the cross-sections of the chambers. The flow velocities were represented by different colors which corresponded to the same scale bar.

In order to obtain a uniform flow pattern, structures of lateral flow chambers were analysed as well as optimized. The depth of the lateral flow chambers were set as 0.37 mm. Boundary conditions of the simulation were the same as that stated above.

Firstly, a most commonly used lateral flow chamber (**Fig. S4 B1**) was evaluated and results were shown in **Fig. S4 B3 and B4**. Although uniformity of the flow velocity was improved compared with that of the axial flow cell, there were still four regions of which the flow velocities were relative small (green colors at the top, bottom, left, and right corner of **Fig. S4 B4**).

Therefore, modifications of the four regions were processed: inflow and outflow channels were moved to the edge of the flow chamber; chamber shape was changed to an oval shape (**Fig. S4 C1**). The final optimized lateral flow chamber had an oval shape with major axis = 20 mm and minor axis = 14 mm, which showed preferred uniformity of flow velocity (**Fig. S4 C3 and C4**). As a result, this chamber structure was applied to fabricating the homemade lateral flow cell (**Fig. 2**).

## 5. Supplementary videos

**Video S1**: Gas retention at the edge of the oval-shaped PDMS flow chamber realized by the homemade lateral flow cell. By using the lateral flow cell that contained an oval-shaped PDMS flow chamber, any unwanted gas from the inflow channel could be kept away from the center of QCM sensor.

**Video S2:** Regeneration of the QCM sensor by flushing the generated gas out of the flow cell with gentle knock. After the gas-phase amplified QCM detection, the generated gas could be flushed out of the lateral flow cell with gentle knock, resulting in an easy regeneration of the QCM sensor.

## References


1. L. M. C. Yang, J. E. Diaz, T. M. McIntire, G. A. Weiss and R. M. Penner, *Analytical Chemistry*, 2008, **80**, 933-943.
2. N. Dixit, K. M. Maloney and D. S. Kalonia, *International Journal of Pharmaceutics*, 2011, **412**, 20-27.
3. E. Härtl, N. Dixit, A. Besheer, D. Kalonia and G. Winter, *European Journal of Pharmaceutics and Biopharmaceutics*, 2013, **85**, 781-789.
4. N. Dixit, K. M. Maloney and D. S. Kalonia, *International Journal of Pharmaceutics*, 2012, **429**, 158-167.